

Numerical evaluation of the influence of porosity on bending properties of 2D carbon/carbon composites

Xujiang Chao^a, Lehua Qi^{*a}, Wenlong Tian^a, Xianghui Hou^c, WenJing Ma^a, Hejun Li^b

- a. School of Mechanical Engineering, Northwestern Polytechnical University, Xi'an 710072, PR China
- b. State Key Laboratory of Solidification Processing, Carbon/Carbon Composites Research Center, Northwestern Polytechnical University, Xi'an 710072, PR China
- c. Faculty of Engineering, University of Nottingham, Nottingham NG7 2RD, United Kingdom.

ABSTRACT:

Numerical simulation with progressive damage criterion is implemented to investigate the effect of porosity on the bending properties of 2D cross-ply carbon/carbon (C/C) composites. The mechanical properties of Pyrocarbon matrix regarding the change of porosity are calculated by using Mori-Tanaka approach. Combining with the stiffness degradation scheme, the ultimate bending strengths are calculated in Abaqus through a user-defined subroutine (USDFLD). Delamination is modelled by inserting cohesive elements between two adjacent plies. A good agreement is obtained when the FEM results are compared to three-point bending experiments. The FEM results show that the bending strength decreases greatly with the increase of porosity. When the porosity reaches up to 18%, the bending strength is decreased by 57%. The major fracture behaviors are interlamination delamination and continuous crack damage in 90° plies. With the increase of porosity, more severe interlamination delamination will be slightly aggravated. In addition, the increase of porosity will also accelerate the damage in 90° plies.

Keywords: 2D C/C composites; Numerical simulation; Flexural properties; Progressive damage

* Corresponding author: Prof. Lehua Qi, [Email: qilehua@nwpu.edu.cn](mailto:qilehua@nwpu.edu.cn) Tel: +86-29- 88460447(o)
Fax: +86-29-88491982

1. Introduction

There is no surprise to claim an essential demand of the accurate mechanical properties characterization for carbon fiber reinforced Pyrolytic carbon (PyC) matrix composites (C/C), which have been applied in the various industries [1, 2] including aircraft brake sinks and aerospace structures even at temperature till 3000 °C due to the excellent properties such as low density, high module, high specific strength and low coefficient of thermal expansion [3, 4]. Chemical vapor infiltration (CVI) [5, 6] has been used to fabricate C/C composites with excellent performance. However, during this process, a large number of pores (voids) are formed resulting from the incomplete infiltration. Since it has been proved that the mechanical properties of the composites are strongly depended on their microstructures [7, 8], the approaches which can precisely characterize the microstructures have obtained significant success on predicting the effective mechanical properties of composites.

Traditionally, experimental measurement is the most commonly used method to investigate the effective mechanical properties of composites [9, 10]. However, due to the time-consuming and costly experimental tests [11], analytical calculation and numerical simulation are at least regarded as an alternative. To date, the analytical models have achieved much progress in investigating the mechanical behaviors of composites [12]. Zuo et al. [13] employed the statistical analytic method and Tsai-Wu polynomial criteria to investigate the tensile strength of 3D braided composites and the results were verified to be accurate. Barbero et al. [14] developed an closed form analytical solution on the basis of mechanics to research the bending properties of balanced laminated composites with matrix cracks.

However, when the effects of the complex microstructures of C/C composites (such as pores and fibers) have to be taken into account, the actual analytical models for predicting the failure behavior require additional specific treatments.

By the availability of advanced commercial FEM package and the powerful scripts interface, FEM simulation has been increasingly used in the last decade [15, 16]. Shi et al. [17] modelled the damage of composites laminates, where Puck progressive damage program [18] was used to define the material properties and Hashin criteria was selected to estimate the breakage of fiber and matrix. Schiffer et al. [19] investigated the bending failure modes of the cross-ply laminate carbon/epoxy composites using the extended FEM technique within the framework of Abaqus/Standard. Rao et al [20] analyzed the effect of architecture on the mechanical properties of 3D C/C composites by FEM simulation, where the geometrical information was gained from the microscopic images. As a result, by using FEM simulation technique, one primary issue is to precisely characterize the microstructures and the properties of the component materials.

To obtain the accurate predictions of the effective mechanical properties of C/C composites with the reasonable computational efficiency, the microstructures of C/C composites should be characterized appropriately. Up to now, extensive techniques have been successfully used to obtain the microstructure of composites, such as scanning electron microscope (SEM) [21], micro CT [11] and Mercury Intrusion Porosimetry (MIP) [22, 23]. Compared with the complex data obtained from micro CT test [24] and only 2D information got from SEM, MIP technique can provide both the distribution of the pore radius and the pore volume [25]. In

the present work, only the effect of porosity on bending properties will be investigated. Hence, by taking into account the computational cost and the result accuracy, MIP technique are selected to characterize the pore inclusions.

The aim of the present work is to evaluate the effect of the porosity on the bending properties of 2D cross-ply C/C composites using FEM simulation technique. The information of the porosity is obtained by the MIP technique. And then, the effective mechanical properties of the unidirectional C/C composites with different porosities are calculated by using two-step M-T mean-field scheme and strength theory. The FEM simulations are implemented in the commercial FE package via a user-defined 3D damage subroutine. Delamination is modelled by inserting the cohesive elements between neighboring plies. The results are validated by comparing against the three-point bend test. Meanwhile, the effects of the porosity on both the ultimate flexural strengths and the fracture behaviors are discussed.

2. Definition of the component materials properties

The 2D C/C composites (fiber volume fraction of 40% with symmetrical cross-ply lamination [0°/90°]) fabricated by the ICVI process (as shown in Fig. 1) are characterized as a complex microstructures (carbon fibers, pores and PyC matrix [26]). Using methane as precursor gas and nitrogen as diluted gas, the preforms are densified at 1100 °C and under a total pressure of 2.5 KPa. The investigated samples are embedded in a resin matrix with polishing, and then microstructures (shown in Fig. 2) of them are characterized by PLM (Leica DMIP PLM). The

pore structures are identified as the black irregular shapes, which distribute in the composites randomly. Besides, there are some initial internal cracks in the composites due to the damage.

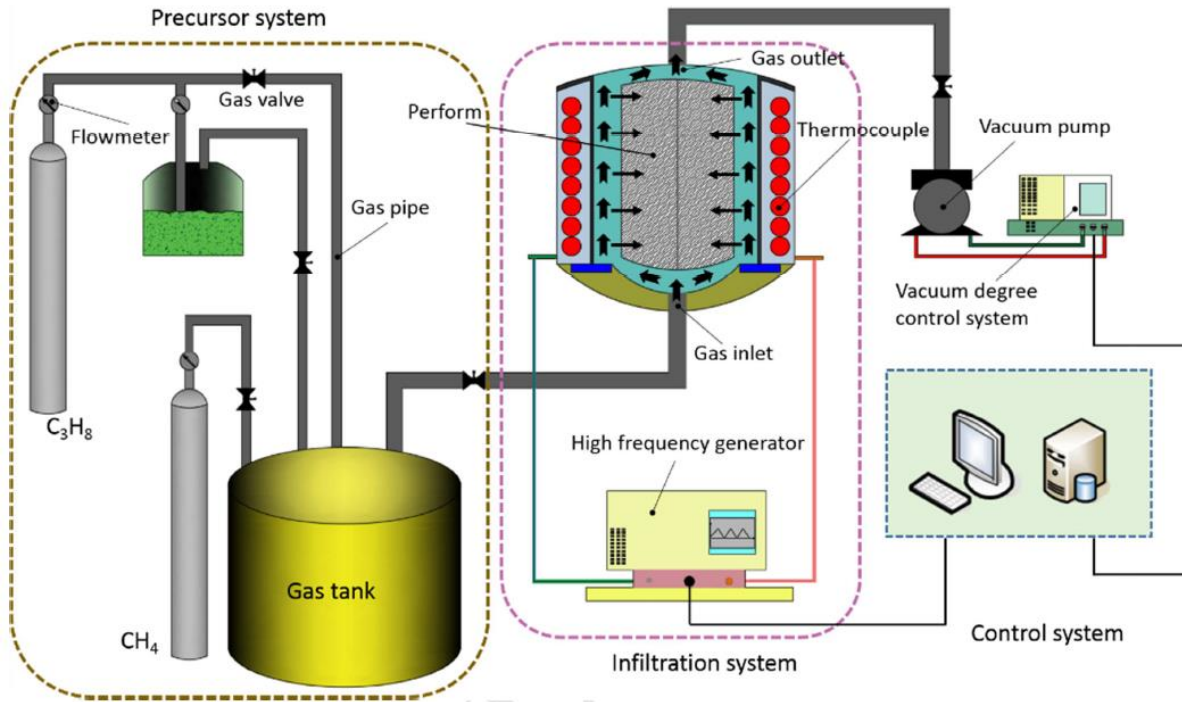


Fig. 1. The CVI principle diagram

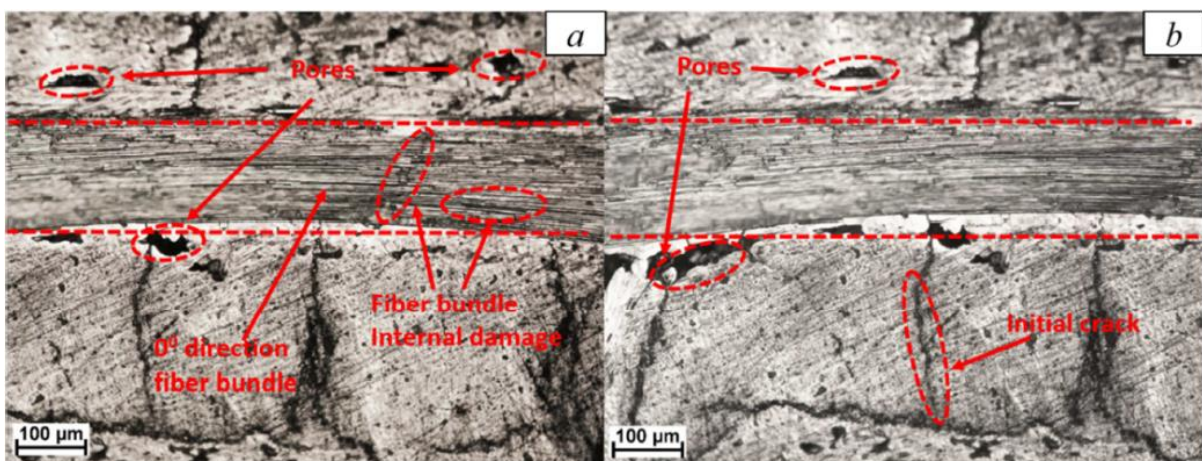


Fig. 2. PLM images of 2D-C/C composites

2.1 Properties of equivalent matrix

The matrix can be regarded as a composites of PyC and void. And the properties of PyC can be measured using the Berkovich head of Nano Indentation technique (G200 NI: BS EN ISO 14577 [27]). Since the size of the head is much smaller than those of the micropores in the C/C composites, the effect of the pore on the test accuracy can be ignore. The strength is measured by uniaxial tensile test (ASTM C1025 and ANSI/ASTM C749), and the results are shown in Table 1.

Table 1. The mechanicals properties of PyC

Material	Elastic modulus E_m (GPa)	Poisson rasion ν_m	Tensile strength (MPa)	Compressive strength (MPa)	Shear strength (MPa)
PyC	12	0.21	14.7	64.7	19.1

In order to define the effective elastic properties of the C/C composites, the distribution of these pores should be tested firstly. However, it is hard to define these irregular structures by using a numerical method. When only the effect of the porosity on the mechanical properties of composites is investigated, it is appropriate to approximate these pore inclusions as spheres.

The volumes of the pores with different radius in the 2D-C/C composites are measured by using the MIP technique (Autopore IV9500 Mercury Porosimetry). The investigated specimens for the pressure mercury tests are cut as $1cm \times 1cm \times 1cm$. Fig. 3(a) shows the five groups test results. In addition, under a certain porosity, the probability density function of the pore radius distribution can be fitted by Logarithmic Gauss function, which is expressed as

$$f(r_i) = \frac{\sum_{j=1}^M V_{ij}}{\sum_{i=1}^N \sum_{j=1}^M V_{ij}} = \frac{1}{r_i \sqrt{2\pi} \delta} \exp \left\{ - \left[\frac{\ln\left(\frac{r_i}{\bar{r}}\right)}{\sqrt{2}\delta} \right]^2 \right\} \quad (1)$$

where $\bar{r} = \sum_{i=1}^N r_i M / NM$ is the weighted average of the pore radius, M is the number of the pores with different radius, N is the number of the radius, and the logarithmic standard

discrete difference of the radius $\delta = \sqrt{\sum_{i=1}^N (r_i^2 - \bar{r}^2) / (N - 1)}$. As a result, \bar{r} and δ are 21.35 μm

and 0.379, respectively.

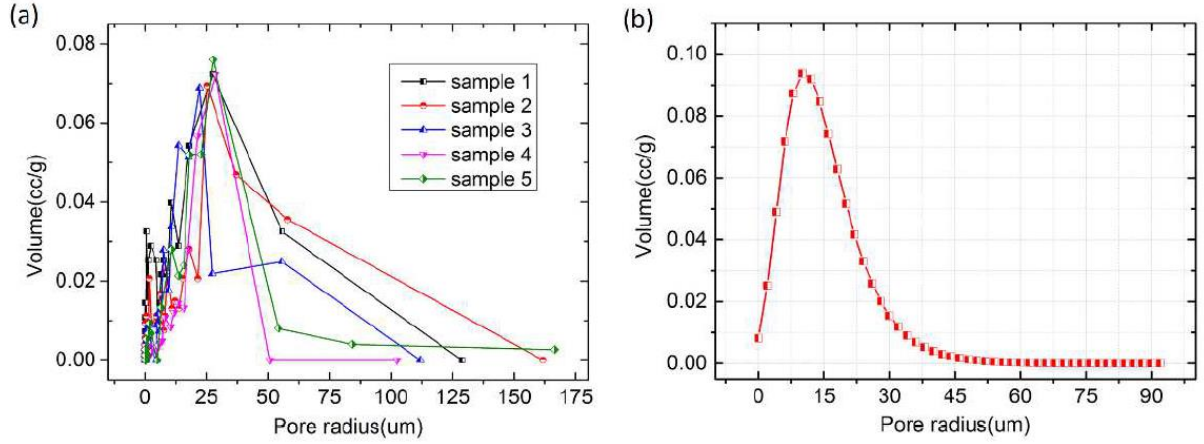


Fig. 3. (a) Relationship between pore volume and pores radius, (b) Probability density distribution of pore radius

In this paper, the C/C composites are considered as a combination of three phase materials (PyC+fiber+pore), and the effective stiffness can be calculated using the two M-T mean-field method [28] as interpreted by Benveniste [29]. In the first M-T step, the equivalent matrix is considered as a composites of two component material (PyC+pore), and the effective compliance tensor is derived as follows,

$$\mathbf{C}^p(\mathbf{S}^I, \mathbf{M}_f, \mathbf{M}_m) = \mathbf{S}^I: [(1 - V_p)(\mathbf{M}_I - \mathbf{M}_m) + \mathbf{S}^I]^{-1}: (\mathbf{M}_I - \mathbf{M}_m) \quad (2)$$

$$\mathbf{M} = \mathbf{M}_m + \mathbf{C}^p \quad (3)$$

where \mathbf{M} , \mathbf{M}_I and \mathbf{M}_m are the compliances of equivalent matrix, inclusion and matrix, respectively. \mathbf{C}^p designates the contribution compliance tensor of the pores. The inclusion stress concentration tensor \mathbf{S}^I is derived as follows,

$$\mathbf{S}^I(\mathbf{I}, \mathbf{M}_f, \mathbf{M}_m) = V_p \left[(\mathbf{M}_I - \mathbf{M}_m)^{-1} + \mathbf{M}_m^{-1}: (\mathbf{I} - \mathbf{S}) \right]^{-1} \quad (4)$$

where \mathbf{I} is the fourth-rank unit tensor ($2\mathbf{I}_{ijkl} = \delta_{ik}\delta_{jl} + \delta_{il}\delta_{jk}$). \mathbf{S} is the Eshelby's tensor which depends on the shape of the inclusion and elastic properties of the matrix [30, 31]. The boldface symbols mentioned throughout this paper designate tensors, the order of which is lucid from the context and the Einstein convention for using the repeated indices.

In addition, the porosity exerts great influence on the strength of the PyC matrix, which can be calculated by the empirical relations [32, 33]. The function relationship between the strength of the matrix and the pore radius is expressed as follows,

$$R = R_0 \left(1 - \pi \sum_{i=1}^N r_i^2 \right) \quad (5)$$

where R_0 is the ultimate strength of the PyC without pores, which can be learned from the reference [34].

2.2 Characterization of carbon fiber after CVI process

Compared with the initial carbon fibers in preforms, the strength parameters of fiber in the composites will decline due to the damage in the preparation process [35] (such as crack and oxidation). The accurate definition of the mechanical properties of carbon fibers after CVI treatment will play an important impact on the prediction of the mechanical properties of C/C composites.

The reinforcement of the 2D-C/C composites is 3K T700 carbon fibers bundle, and the strengths of which after CVI process are measured by the uniaxial tension tests. Because the mechanical properties of the bundles are not fully consistent, a statistical theory on the basis of chain model is proposed to characterize the average strength of the boundless, which assumes that the strengths of the brittle fibers can be described by the unimodal Weibull function [36, 37],

$$F(\sigma)=1-\exp\left[-D\left(\frac{\sigma}{\alpha}\right)^{\beta}\right] \quad (6)$$

where $F(\sigma)$ is the fracture probability of a fiber under the stress σ , α and β are the Weibull scale parameter and shape parameter, respectively, D is the volume of fibers under stress. Suppose that the total number of fibers in a bundle is K . $\sigma_i(i=1,2,\dots,K)$ is the strength of fibers, and the average fiber strength as a function of Weibull parameters can be presented as,

$$\bar{\sigma}=\alpha\Gamma\left(1+\frac{1}{\beta}\right)D^{-1/\beta} \quad (7)$$

where $\Gamma(1+\beta)$ is Gamma function. With the increase of the fibers number K in the bundle, or even $K \rightarrow \infty$, the strength of the fiber bundles can be represented using Gauss function [38]. Thus, the probability density and the cumulative distribution function are derived respectively,

$$f(\sigma_{str}) = \frac{1}{\delta\sqrt{2\pi}} \exp\left[-\frac{(\sigma_{str} - \bar{\sigma}_a)^2}{2\delta^2}\right] \quad (8)$$

$$F(\sigma_{str}) = \int_0^{\sigma_{str}} f(\sigma_{str}) d\sigma_{str} \quad (9)$$

where a and d are the mean value and standard deviation of the fiber bundles strength, respectively. According to the results of uniaxial tension tests of the fiber bundles after CVI process treatment and Eq. (8-9), a and d are 1237 MPa and 14.8, respectively.

3. FEM simulation

This section describes the details of the FEM simulation. The algorithm outlined in Section 2 is used to define the materials properties of the FEM models. Combining with the failure criteria and stiffness degradation program, the bending properties of the 2D-C/C composites are obtained by using the FEM software and script interface. The process of the simulation and calculation is shown in Fig. 4.

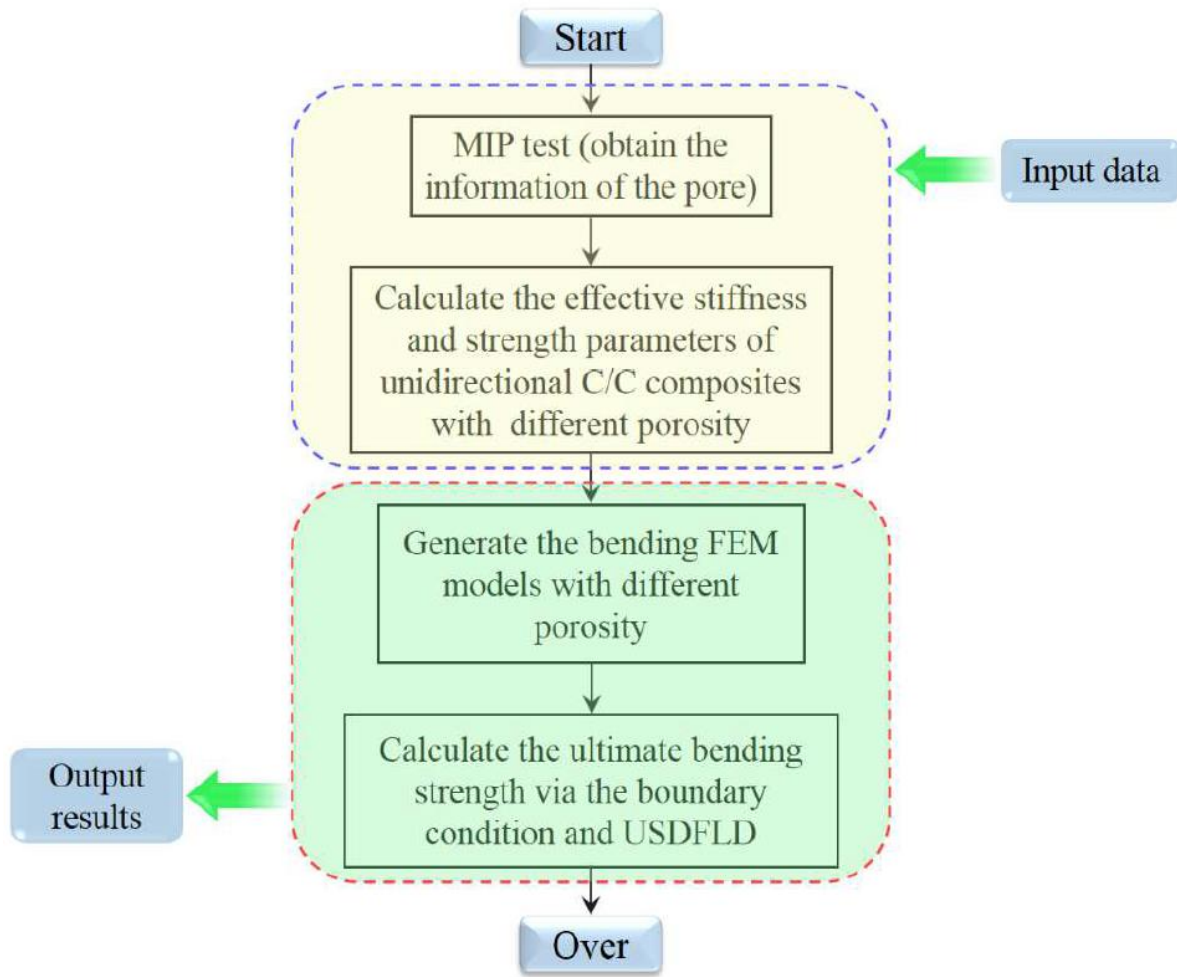


Fig. 4. Flow chart of the process of the simulation and calculation

3.1. Generation of the FEM mode

The FEM models of the 2D-C/C composites established to simulate the static flexural mechanical properties are rectangular prism with dimensions of $L \times b \times h = 55 \times 8 \times 4 \text{ mm}^3$ (Fig. 5).

The span (L_s) between two supports is 40 mm. Both the supports and the pressure head are defined as discrete rigid, and the radius are 5 mm.

The composites parts are meshed using 8-node linear brick element (C3D8R in Abaqus/Standard (2014a)) with the reduced integration and hourglass control, and the

interface between two adjacent plies are meshed using the COH3D8 cohesive elements. Based on the standard discretization, the relatively finer mesh (with 27,600 elements of the composites part) provides the very close simulation results and it is supposed that the satisfied standard discretization is good enough. Both the global and local coordinates are defined to interpret the ply orientation and to accurately describe the laminate composites mechanical behaviors. Meanwhile, the pressure head and the supports are meshed by using the quadrilateral discrete rigid elements.

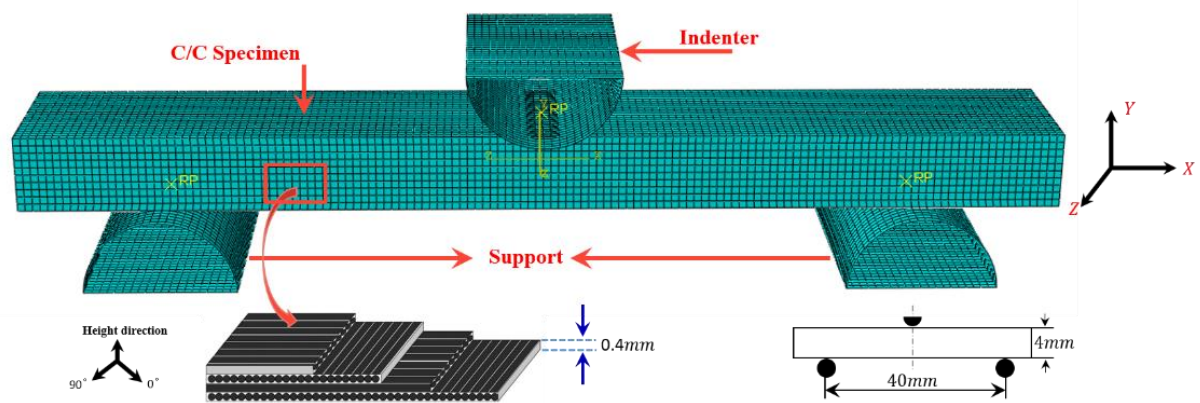


Fig. 5 Mesh diagram for three point bending FEM

3.2 Failure criteria and Stiffness degradation program

3.2.1 Failure criteria of 2D-C/C composites

In the failure process of fiber reinforced composites, there are several different damage types including fiber failure, matrix failure and interlaminar debonding failure [39]. Thus, in the FEM simulation, failure criteria is important to obtain the accurate materials properties. Tsai-Wu polynomial criteria [13, 40] has been successfully adopted as a fracture criterion in the

laminates composites, which can be cast into a more familiar tensor polynomial expression of Eq. (10).

$$F_i \sigma_i + F_{ij} \sigma_i \sigma_j + F_{ijk} \sigma_i \sigma_j \sigma_k + \dots = 1 \quad (10)$$

where $i, j, k, \dots = 1, 2, \dots, 6$. And $\sigma_4 = \tau_{23}$, $\sigma_5 = \tau_{31}$, $\sigma_6 = \tau_{12}$, therefore, the stress $[\sigma] = [\sigma_1, \sigma_2, \sigma_3, \tau_{23}, \tau_{31}, \tau_{12}]^T$. For orthotropic 2D-C/C composites, second-tensor of the Tsai-Wu polynomial rule is chosen as the failure criteria.

$$F_{11} \sigma_1^2 + F_{22} \sigma_2^2 + F_{33} \sigma_3^2 + F_{44} \sigma_4^2 + F_{55} \sigma_5^2 + F_{66} \sigma_6^2 + 2F_{12} \sigma_1 \sigma_2 + 2F_{13} \sigma_1 \sigma_3 + 2F_{23} \sigma_2 \sigma_3 + F_1 \sigma_1 + F_2 \sigma_2 + F_3 \sigma_3 = 1 \quad (11)$$

where F_i and F_{ij} can be derived as follow,

$$\begin{aligned} F_1 &= \frac{1}{X_T} - \frac{1}{X_C}, F_2 = \frac{1}{Y_T} - \frac{1}{Y_C}, F_3 = \frac{1}{Z_T} - \frac{1}{Z_C}, F_{11} = \frac{1}{X_T X_C}, F_{22} = \frac{1}{Y_T Y_C}, F_{33} = \frac{1}{Z_T Z_C}, F_{44} \\ &= \frac{1}{S_{23}^2}, F_{55} = \frac{1}{S_{31}^2}, F_{66} = \frac{1}{S_{12}^2}, F_{12} = \frac{-1}{2\sqrt{X_T X_C Y_T Y_C}}, F_{23} = \frac{-1}{2\sqrt{Y_T Y_C Z_T Z_C}}, F_{31} \\ &= \frac{-1}{2\sqrt{Z_T Z_C X_T X_C}} \end{aligned} \quad (12)$$

where X_T and X_C are the tensile and compression strengths of the unidirectional laminate in the fiber direction, Y_T and Y_C are the transverse tensile and transverse compression strengths, S_{12} , S_{13} , and S_{23} denote the in-plane and out-plane shear strengths, respectively. Under each loading condition, substitute the stresses of the elements into Eq. (11). If the element is determined to be failed, then the stiffness of it will degrade according to the corresponding failure modes. The judgment of the stress state and the stiffness degradation program will be repeated, until the laminate composites part fails.

3.2.2 Definition of stiffness degradation program

When the stress of the element satisfies the failure criterion of Eq. (11), there are several different stiffness degradation programs corresponding to various damage modes. Considering the in-situ effect of laminate composites, Puck [18] proposed a method to determine the degradation coefficient Q_d , which is listed in Table 2. The flow chart of the stiffness degradation principle is shown in Fig. 6.

Table 2. Stiffness degradation coefficient under different failure mode

Failure mode	Stiffness degradation coefficient
Delamination ($\sigma_{33} \geq 0$)	$Q_d = 0.1Q(Q = E_{33}, G_{13}, G_{23}, \nu_{13}, \nu_{23})$
Delamination ($\sigma_{33} < 0$)	$Q_d = 0.1Q(Q = E_{33}, G_{13}, G_{23}, \nu_{33}, \nu_{23})$
Matrix tensile failure	$Q_d = 0.2Q(Q = E_{22}, G_{12}, G_{23}, \nu_{12}, \nu_{23})$
Matrix compression failure	$Q_d = 0.4Q(Q = E_{22}, G_{12}, G_{23}, \nu_{12}, \nu_{23})$
Fiber tensile failure	$Q_d = 0.07Q(Q = E_{11}, G_{12}, G_{13}, \nu_{12}, \nu_{13})$
Fiber buckling failure	$Q_d = 0.14Q(Q = E_{11}, G_{12}, G_{13}, \nu_{12}, \nu_{13})$

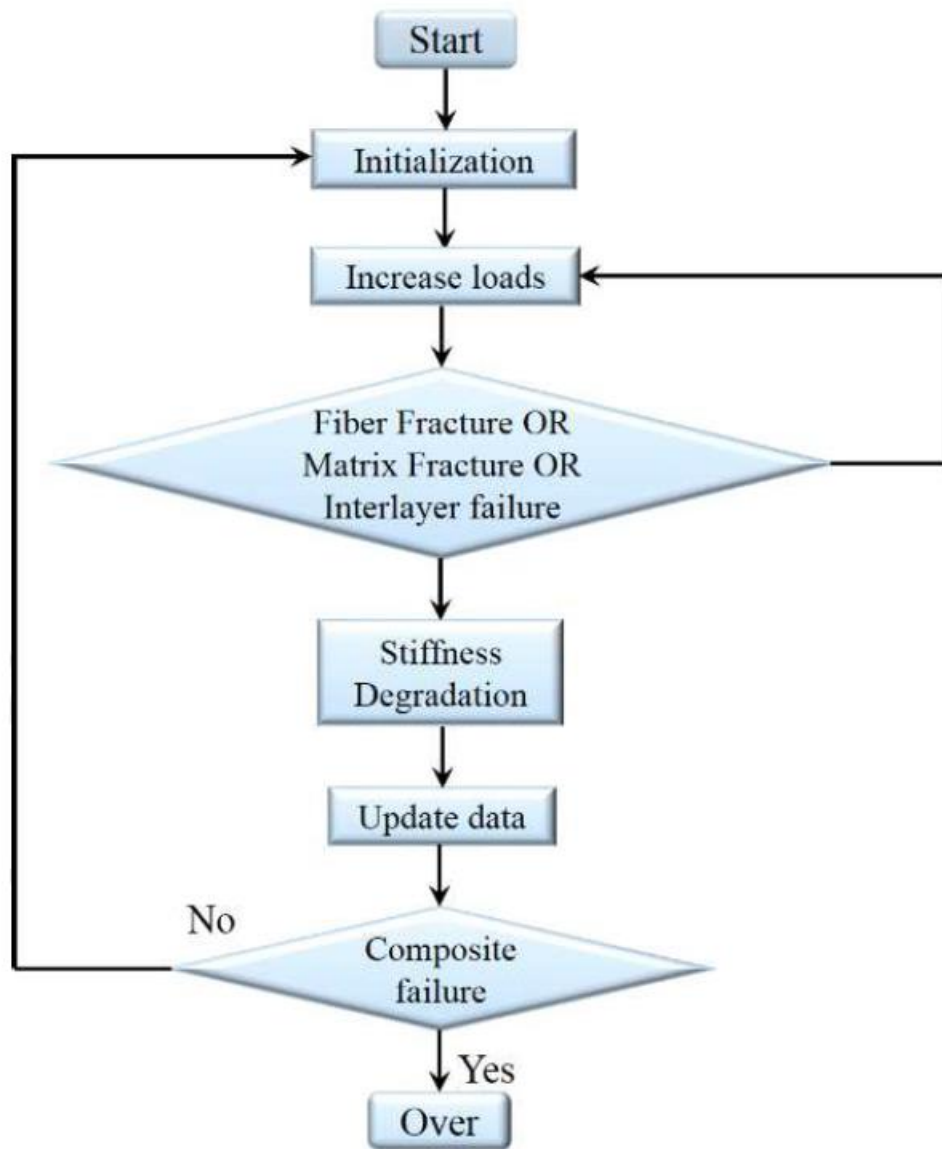


Fig. 6 Flow chart of stiffness degradation

3.2.3 Damage law for interface elements

The interface between the adjacent two plies of laminates is defined by the 0 thickness cohesive elements (Fig. 7(c)). In this approach, an interface is considered as an independent material joining the adjacent piles of the laminates and has its own constitutive law. A typical traction-separation response (Fig. 7 (a), (b)) is used as the damage initiation criterion and it assumes a linear elastic behavior followed by the initiation and evolution of damage [17]. In

this paper, damage initiation is defined with the use of quadratic nominal stress criterion which is shown as,

$$\left(\frac{\langle \tau_3 \rangle}{N}\right)^2 + \left(\frac{\tau_1}{S}\right)^2 + \left(\frac{\tau_2}{T}\right)^2 = 1 \quad (13)$$

where τ_i ($i=1, 2, 3$) denotes the traction stress vector in two shear and normal directions, respectively. N, S, T are the corresponding inter-laminate normal and shear strengths and T is usually assumed equal to S ($S=T$). $\langle \bullet \rangle$ is the Macaulay bracket.

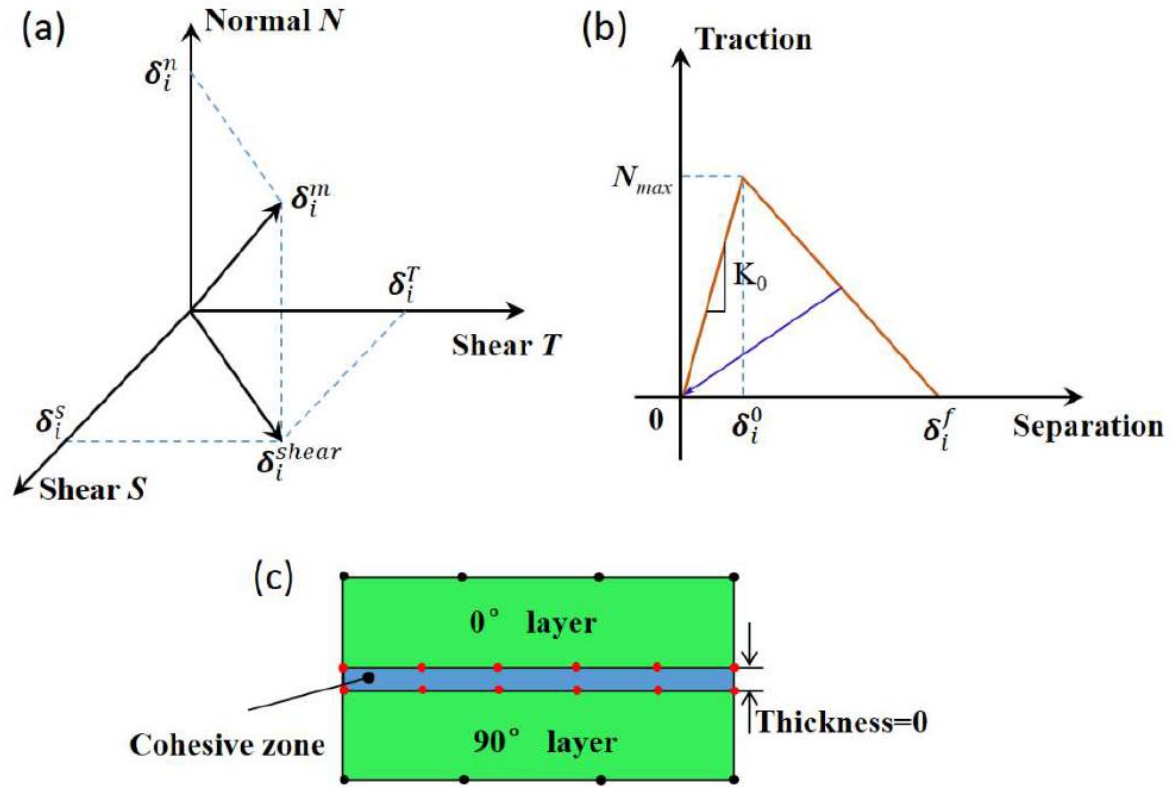


Fig. 7 (a) Traction-separation relationship under mixed fracture mode, (b) Traction-separation behavior of the cohesive model, (c) Schematic of cohesive zone

Progressive damage of the interface occurs according to the evolution law when the mixed-mode damage has initiated. Benzeggagh-Kenane (B-K) [41] fracture criterion is used to predict the evolution delamination under mixed-mode [42],

$$G_C = G_{IC} + (G_{IIC} - G_{IC}) \left(\frac{G_S}{G_T} \right)^\eta \quad \text{with} \quad G_S = G_{II} + G_{III} \quad (14)$$

where $G_T = G_I + G_S$, G_{IC} and G_{IIC} are the fracture toughness of model I and model II, respectively. η is a parameter of the B-K power law, which is determined by the material property. The total mixed-mode displacement δ_m can be expressed as.

$$\delta_m = \sqrt{\delta_1^2 + \delta_3^2 + \langle \delta_3 \rangle^2} = \sqrt{\delta_s^2 + \langle \delta_3 \rangle^2} \quad (15)$$

Furthermore, for a softening process the damage variable d can be defined as,

$$d = \frac{\delta_m^f (\delta_m^{\max} - \delta_m^0)}{\delta_m^{\max} (\delta_m^f - \delta_m^0)} \quad (16)$$

where δ_m^{\max} is the maximum effective displacement of the mixed-mode jump in loading history. δ_m^0 and δ_m^f are the damage onset and final displacement jump at mixed-mode loading (Fig. 7(a) and (b)), respectively. Initially, the linear elastic properties are defined as K_i ($i=1, 2, 3$). Once the normal or shear tractions reach the corresponding normal and shear strengths, the stiffness will degrade linearly according to the damage evolution variable d as Eq. (16). The normal and shear strengths of the interface are 45MPa and 60MPa, respectively, and the fracture toughness for the interface $G_{IC}=0.5\text{KJ/m}^2$, $G_{IIC}=0.7\text{KJ/m}^2$, $\eta=2$ [43, 44].

3.3 Materials, loading and boundary conditions

The 2D C/C composites can be considered as a combination of unidirectional C/C composites with different orientation (0° and 90°). The effective stiffness of the unidirectional C/C composites (equivalent matrix+fiber) can be calculated using the second M-T method, in which the identical fibers are regarded as unidirectional cylindrical inclusions,

$$\mathbf{M}_{eff} = \mathbf{M} + \mathbf{C}^f \quad (17)$$

where \mathbf{M}_{eff} and \mathbf{C}^f are the compliance tensor of the unidirectional composites and the contribution compliance contribution tensor of fiber inclusions, respectively. As discussed in Eq. (2) and (4), the compliance tensor of the identical column inclusion is determined by the elastic properties of the component materials and Eshelby's tensor of the cylindrical inclusions [30]. Meanwhile, the effective strength parameters can be calculated on the basis of a strength theory by using the strengths parameters of components materials (equivalent matrix and fibers) and the effective elastic properties of the unidirectional C/C composites [45, 46]. In this theory, it postulates that the composites is considered to fail whenever any of its constituent materials, either the fiber or the matrix, attain its ultimate stress. Moreover, the fiber material is linearly elastic until rupture and there is a perfect bonding along the interface between the fiber and matrix. For the unidirectional C/C composites under compression load, the main failure modes of it are the instability of fiber and the collapse of matrix, and the longitudinal strength and the transverse strength can be calculated by using the fraction values of the component materials, the strength of the matrix and the elastic properties of the matrix

and reinforcement [47, 48]. The effective properties of the unidirectional C/C composites with no pores are listed in Table 3.

Table 3. The properties of the unidirectional C/C composites with no voids

E_{11}	$E_{22}=E_{33}$	$\nu_{12}=\nu_{13}$	ν_{23}	$G_{12}=G_{13}$	G_{23}
119.2 GPa	24.86 GPa	0.226	0.403	7.522 GPa	7.264 GPa
X_T	X_C	$Y_T=Z_T$	$Y_C=Z_C$	$S_{12}=S_{13}$	S_{23}
422.36 MPa	8.26 MPa	12.96 MPa	38.1 MPa	17.9 MPa	12.8 MPa

The contact condition between the pressure head and the composites part is surface-to-surface with small displacement, and the friction coefficient is chosen as 0.2 [17]. In order to mimic the boundary conditions of the experiments, the right and left supporters are defined to be coupled with the composites part and the contact conditions between them are rigid. The boundary conditions are defined by constraining all degrees of freedom of the supporters. In order to make the calculation process easy to converge, the loading conditions of the model are divided into two steps. In the first step, a very small displacement load (0.001 mm) is applied to the reference point of the head, and then in the second step, a displacement load (1.2 mm) is applied which ensures the failure of the composites part. Consequently, following by the simulation models generated in the commercial FEM package Abaqus by importing the aforementioned porous materials properties via Python interface [49], the bending properties of the 2D cross-ply C/C composites are calculated.

4. Results and discussion

4.1 Effect of the porosity on the flexural strength

The reaction force and the displacement of the reference point are obtained by solving the FEM models generated above. During the bending process, due to the maximum bending deflection (δ_M) of the composites part $\delta_M/L_s \ll 0.1$, the bending stresses can be calculated by the reaction force of reference point,

$$\sigma_b = \frac{3\mathbf{R}_F L_s}{2bh^2} \quad (18)$$

where \mathbf{R}_F is the reaction force corresponding to the displacement load applied in the reference point. In our previous research, to meet the application requirement, the porosity of the C/C composites prepared by CVI is usually less than 20%. In this study, the porosity of the models are chosen as follows: (1) $V_p=0$; (2) $V_p=0.03$; (3) $V_p=0.06$; (4) $V_p=0.09$; (5) $V_p=0.12$; (6) $V_p=0.15$; (7) $V_p=0.18$. Therefore, the bending strengths of these models can be derived by the maximum reaction force $\mathbf{R}_{F_s}=\max\langle\mathbf{R}_F\rangle_{i=1, 2, \dots, n}$ during the process of bending deformation. In addition, there are five groups of static bending tests of 2D cross-ply C/C composites with different porosities, which are measured by INSTRON 8872 at a constant loading speed of 0.5 mm/min with span of 40 mm.

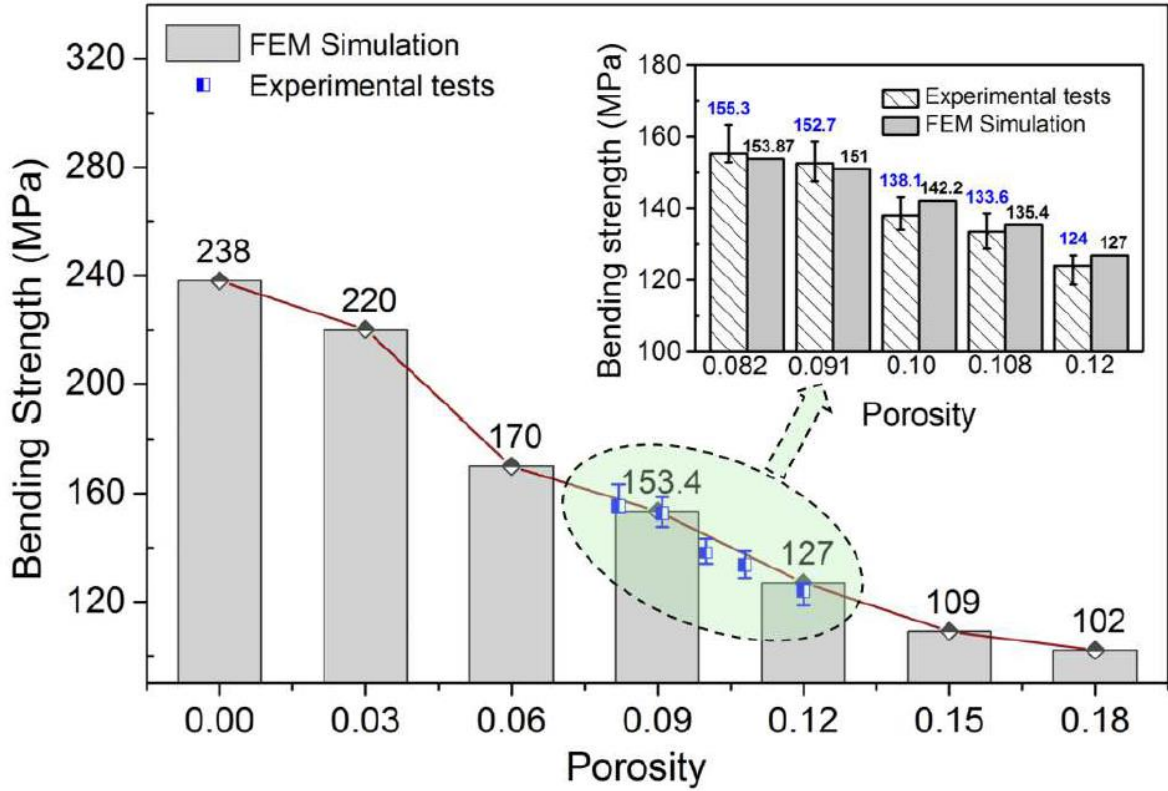


Fig. 8. The Flexural strength regarding the change in porosity

Fig. 8 illustrates the results of the FEM simulation and experimental tests. It can be observed that the results from the three-point bending tests are in good agreement with those from numerical simulations, and the maximum difference is $d = \langle \max \rangle_{i=1,2,3} = \|\sigma_{bs} - \sigma_{bt}\| / \sigma_{bs} = 2.82\%$. For the higher porosity values of the C/C composites, similar conclusions can also be found in the Ref [50]. The FEM results show that with the increase of the porosity, the flexural strength of 2D-C/C composites decrease rapidly. When the porosity reaches up to 12%, the bending strength is decreased by 46.6%. Since then, with the further increase of porosity, the downward trend of the bending strength will slow down, and finally when the porosity reaches up to 18%, the bending strength decreases by 57%. All the results show that the bending strength of 2D-C/C composites depends on the pore greatly.

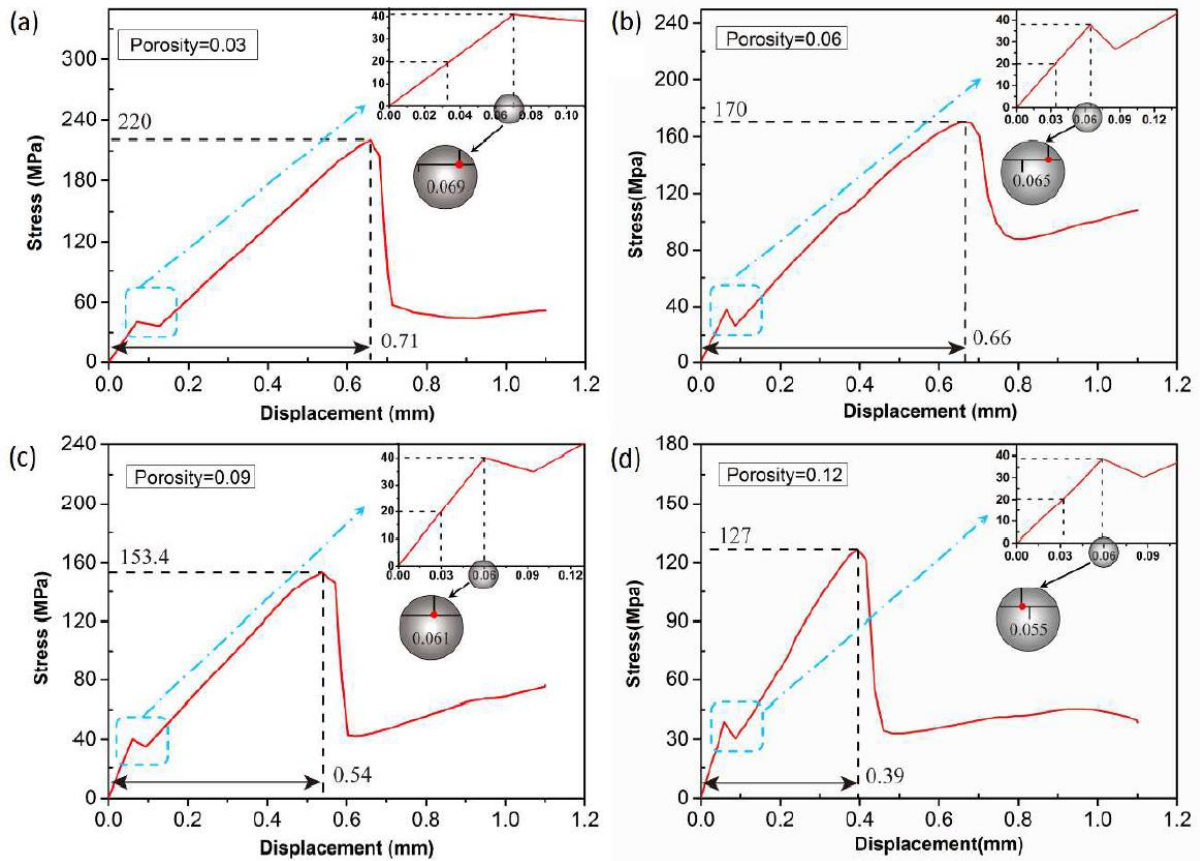


Fig. 9. Stress regarding the change in the load displacement (a) porosity=0.03, (b) porosity=0.06, (c) porosity=0.09, (d) porosity=0.12

Fig. 9 shows the relationship between the displacement and the stress of the reference point. For the porosity of 3%, 6%, 9% and 12%, it can find that there are two drastic stress drop in the stress-displacement curves, respectively, and the displacements corresponding to the initial stiffness degradation also slightly decreases with the increasing of the porosity. Moreover the failure displacement of the models decreases with the increase of the porosity.

4.2 Influence of porosity on the bending fracture behaviour

C/C composites exhibit a relatively brittle or pseudo plastic fracture behavior due to the brittle properties of component materials (carbon fibers and PyC matrix). Fig. 10 illustrates several typical fracture features of the investigated specimens after three-point bending tests, including delamination and continuous crack in 90° ply. With the increase of bending loading, the initial debonding damage occurs at the interface between adjacent two layers due to the weaker interface strength. The deboned interface loses the load transferring capacity. Following the increasing loading, crack formed in 90°-ply, which results from the weaker bearing capacity compared with the 0°-ply in the loading direction.

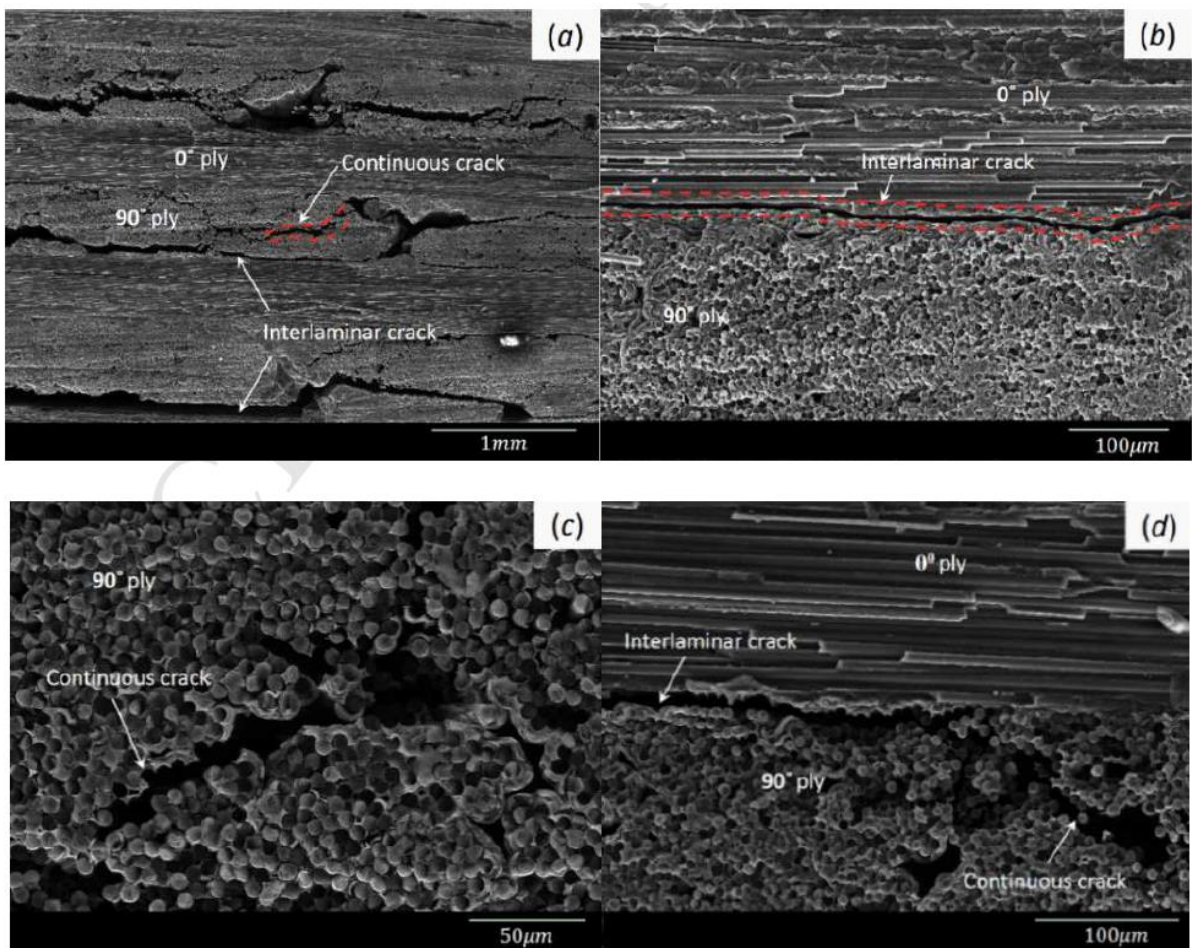


Fig. 10. The typical SEM images of fracture specimens after three-point bending test

During the bending simulations, there are several damage models including fiber breakage, matrix damage and interlaminar debonding, which are defined by the proposed initiation and progression fracture criteria through FORTRAN user-defined subroutine (USDFLD). The results show that interlaminar delamination and damages in 90° plies are the main fracture modes (Fig. 11), which are also found in Fig. 10.

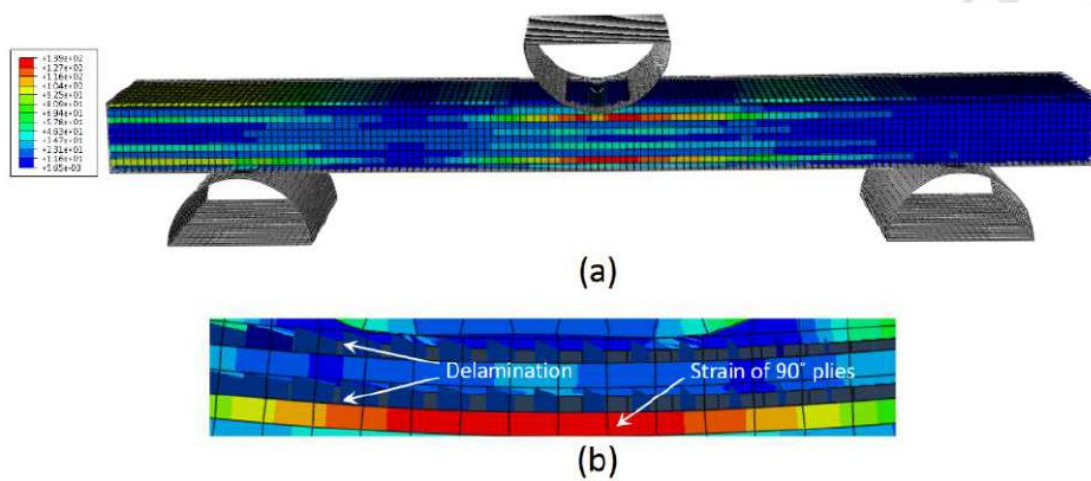


Fig. 11. Damage modes of 2D C/C composites subjected to bending load. (a) Initial contact, (b) Bending failure

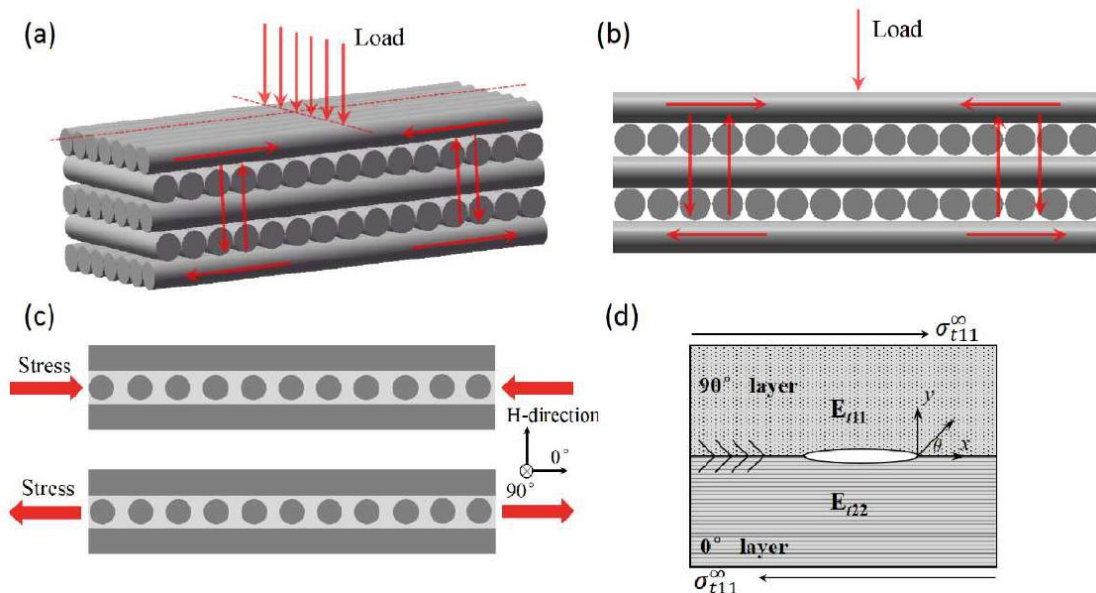


Fig. 12. (a), (b), (c) Loading diagram in 2D cross-ply C/C composites models, (d) Interface crack between two orthotropic materials

The loading diagram of 2D C/C composites during the bending simulation is shown in Fig. 12. As shown in the diagram, upper plies bear compressive stress and lower plies bear tensile stress during the bending process. For the lower adjacent layers who subject to the tensile stress, the energy release rate of the crack at the interface of the cross-ply laminates with equal thickness plies can be written as [51, 52],

$$G = \frac{(1 - \mathbb{R}^2)}{\mathbf{E}^*} |\mathbf{K}|^2 \quad (19)$$

where \mathbf{K} is the stress intensity factor corresponding to the crack-tip at interface (Fig. 12(d)), which is determined by the stress state and geometric parameters of the two materials 0° and 90° plies. \mathbb{R} and \mathbf{E}^* can be given as,

$$\begin{cases} \mathbb{R} = \frac{1}{2} \frac{\mu_{0^\circ\text{-ply}}(1 - 2\nu_{21}) - \mu_{90^\circ\text{-ply}}(1 - 2\nu_{12})}{\mu_{0^\circ\text{-ply}}(1 - \nu_{21}) - \mu_{90^\circ\text{-ply}}(1 - \nu_{12})} \\ \mathbf{E}^* = \frac{1}{2} \left(\frac{1}{\bar{\mathbf{E}}_{t11}} + \frac{1}{\bar{\mathbf{E}}_{t22}} \right) \end{cases} \quad (20)$$

where $\bar{\mathbf{E}}_i = \mathbf{E}_i / (1 - \nu_i^2)$. μ is the shear modulus of the respective 0° -ply and 90° -ply.

Substituting Eq. (20) into (19), the energy release rate of the interface crack can be derived as,

$$G = h(\nu_i) \frac{\mathbb{C} - \left(\frac{\mathbf{E}_{t11} - \mathbf{E}_{t22}}{\mathbf{E}_{t11} + \mathbf{E}_{t22}} \right)^2}{(\mathbf{E}_{t11} + \mathbf{E}_{t22}) / (\mathbf{E}_{t11} \cdot \mathbf{E}_{t22})} \quad (21)$$

where \mathbf{E}_{t11} and \mathbf{E}_{t22} are the elastic modulus along the fiber direction and vertical fiber direction in the 0° ply, respectively. \mathbb{C} is a constant and h is a function of Poisson's ratio. Compared with the change of the elastic modulus, the variation of the Poisson's ratio can be neglected. Therefore, h can be also regarded as constant here. With the increase of the pore

volume fraction, E_{t11} and E_{t22} decrease as a result of E_m reducing to ΔE_m . It can be found from Eq. (21), the energy release rate (G) of the crack at the ply interface slightly decreases with the increase of porosities. And the delamination fracture accelerate slightly. Similarly, the porosity also effects the delamination of upper plies.

Compared to the 0° plies, the ultimate capacity of the 90° plies is smaller due to the load perpendicular to the fiber direction, which will contribute to the occurrence of damages in the transverse plies easily. During the bending process, the initial crack nucleus could form at the location of the pores or defects in the PyC matrix. With the increase of the bending load, these crack nucleus in the 90° plies begin to extend along the transverse and thickness directions, which are defined as L and T shape of mode **I** cracks (Fig. 13). Eventually, a continuous inclined slit crack parallel to the transverse fiber will be formed in the 90° plies. For the orthotropic materials, the strain energy of these transverse cracks can be given by Eq (22a), and the strain energy release rate of L and T cracks can be derived using Eq (22b) and (22c) [53], respectively.

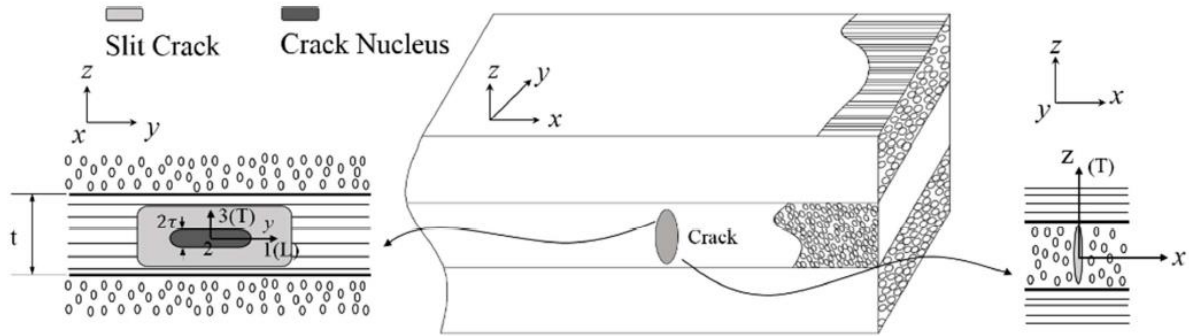
$$U = \frac{1}{2}\pi\tau^2 \left\{ \Lambda_{22}^0 \sigma_{t22}^0 + 2 \int_0^{\gamma_{12}} \sigma_{12} d\gamma_{12} \right\} = \frac{1}{2}\pi\tau^2 \{ \Lambda_{22}^0 \sigma_{t22}^0 + \chi(\gamma_{12}) \} \quad (22a)$$

$$G(\mathbf{T}) = -\frac{1}{2} \frac{\partial U}{\partial \tau} = \frac{\pi\tau}{2} \Lambda_{22}^0 \sigma_{t22}^2 \quad (22b)$$

$$G(\mathbf{L}) = \frac{U}{2\tau} = \frac{\pi\tau}{4} \Lambda_{22}^0 \sigma_{t22}^2 \quad (22c)$$

Where $\Lambda_{22}^0 = 2(1/E_{t11} - \nu_{21}^2/E_{t22})$ and γ_{12} is the in-plane shear strain. It is consistent with the conclusion drawn above. With the increase of porosity, the relative reduction of E_{t22} is

greater than E_{t11} , so the strain energy release rate of $G(T)$ and $G(L)$ decrease. Therefore, the expansion of transverse cracks will be easier with the ascending of the porosity and the transverse fractures phenomenon increase.



5. Conclusions

A strategy has been presented to evaluate the effective flexural properties and fracture behaviors of the 2D cross-ply C/C composites with porosity. The relationship between porosity and pore radius are measured by means of MIP technique and Gauss numerical fitting method. The effective mechanical properties of the unidirectional C/C composites with different porosities are calculated by using two-step M-T mean-field scheme and strength theory, which serve as input data for generating the bending FEM models via the Python scripts. The ultimate bending strengths are obtained by implementing a user-defined 3D damage model into the subroutine of the finite element code Abaqus. Meanwhile, the bending strengths of 2D C/C composites with different porosities captured by the proposed numerical model are compared with the results measured by three-point bending tests, which are in good agreement.

FEM results show that the bending strength decrease greatly with the increase of porosity. When the porosity reaches up to 18%, the bending strength decreases by 57%. Meanwhile, during the bending failure, the major fracture behaviors are delamination and damage in 90° plies. With the increase of porosity, the interlaminar delamination fracture will be slightly aggravated. Moreover, the increase of porosity will accelerate the damage in 90° plies.

Acknowledgment

The authors wish to thank the National Nature Science Foundation of China under grant No. 51472203 and 51432008.

References

- [1] Fitzer E. The future of carbon-carbon composites. *Carbon*. 1987;25(2):163-90.
- [2] Windhorst T, Blount G. Carbon-carbon composites: a summary of recent developments and applications. *Materials & Design*. 1997;18(18):11-5.
- [3] Liu Y, Fu Q, Zhao F, Sun G, Li H. Internal friction vs. thermal shock in C/C composites. *Composites Part B: Engineering*. 2016;106:59-65.
- [4] Morgan P. *Carbon fibers and their composites*: CRC press; 2005.
- [5] Reznik B, Gerthsen D, Hüttinger K. Micro-and nanostructure of the carbon matrix of infiltrated carbon fiber felts. *Carbon*. 2001;39(2):215-29.
- [6] Benzinger W, Hüttinger K. Chemistry and kinetics of chemical vapor infiltration of pyrocarbon–VI. Mechanical and structural properties of infiltrated carbon fiber felt. *Carbon*. 1999;37(8):1311-22.
- [7] Khezzzadeh H. A statistical micromechanical multiscale method for determination of the mechanical properties of composites with periodic microstructure. *Composites Part B: Engineering*. 2017;115:138-43.
- [8] Hao M-y, Luo R-y, Xiang Q, Hou Z-h, Yang W, Shang H-d. Effects of fiber-type on the microstructure and mechanical properties of carbon/carbon composites. *New Carbon Materials*. 2014;29(6):444-53.
- [9] Hernández S, Sket F, González C, LLorca J. Optimization of curing cycle in carbon fiber-reinforced laminates: void distribution and mechanical properties. *Compos Sci Technol*. 2013;85:73-82.
- [10] Okereke MI. Flexural response of polypropylene/E-glass fibre reinforced unidirectional composites. *Composites Part B*. 2016;89:388-96.

- [11] Sharma R, Deshpande VV, Bhagat AR, Mahajan P, Mittal RK. X-ray tomographical observations of cracks and voids in 3D carbon/carbon composites. *Carbon*. 2013;60:335-45.
- [12] Fan Y, Wang H. Nonlinear bending and postbuckling analysis of matrix cracked hybrid laminated plates containing carbon nanotube reinforced composite layers in thermal environments. *Composites Part B: Engineering*. 2016;86:1-16.
- [13] W. Z, L. X, D. L. Statistical strength analyses of the 3-D braided composites. *Compos Sci Technol*. 2007;67(10):2095-102.
- [14] Barbero EJ, Cabrera Barbero J. Analytical Solution for Bending of Laminated Composites with Matrix Cracks. *Composite Structures*. 2016;135:140-55.
- [15] Reinoso J, Paggi M, Blázquez A. A nonlinear finite thickness cohesive interface element for modeling delamination in fibre-reinforced composite laminates. *Composites Part B*. 2016;109:116-28.
- [16] Aluko O, Gowtham S, Odegard GM. Multiscale modeling and analysis of graphene nanoplatelet/carbon fiber/epoxy hybrid composite. *Composites Part B: Engineering*. 2017;131:82-90.
- [17] Shi Y, Pinna C, Soutis C. Modelling impact damage in composite laminates: a simulation of intra-and inter-laminar cracking. *Composite Structures*. 2014;114:10-9.
- [18] Puck A, Schürmann H. Failure analysis of FRP laminates by means of physically based phenomenological models. *Compos Sci Technol*. 2002;62(12):1633-62.
- [19] Schiffer A, Tagarielli VL. Predictions of the interlaminar tensile failure of a carbon/epoxy composite laminate. *Composite Structures*. 2015;133:997-1008.
- [20] Rao MV, Mahajan P, Mittal R. Effect of architecture on mechanical properties of carbon/carbon composites. *Composite Structures*. 2008;83(2):131-42.
- [21] Tong Y, Bai S, Chen K. C/C–ZrC composite prepared by chemical vapor infiltration combined with alloyed reactive melt infiltration. *Ceramics International*. 2012;38(7):5723-30.
- [22] Abell AB, Willis KL, Lange DA. Mercury Intrusion Porosimetry and Image Analysis of Cement-Based Materials. *Journal of Colloid and Interface Science*. 1999;211(1):39-44.
- [23] Nam J, Kim G, Lee B, Hasegawa R, Hama Y. Frost resistance of polyvinyl alcohol fiber and polypropylene fiber reinforced cementitious composites under freeze thaw cycling. *Composites Part B: Engineering*. 2016;90:241-50.
- [24] Drach B, Tsukrov I, Gross T, Dietrich S, Weidenmann K, Piat R, et al. Numerical modeling of carbon/carbon composites with nanotextured matrix and 3D pores of irregular shapes. *Intl J Solids Struct*. 2011;48(18):2447-57.
- [25] Wu Q, Zhu W, Zhang C, Liang Z, Wang B. Study of fire retardant behavior of carbon nanotube membranes and carbon nanofiber paper in carbon fiber reinforced epoxy composites. *Carbon*. 2010;48(6):1799-806.
- [26] Guellali M, Oberacker R, Hoffmann MJ. Influence of the matrix microstructure on the mechanical properties of CVI-infiltrated carbon fiber felts. *Carbon*. 2005;43(9):1954-60.
- [27] Iso BSEN. Metallic materials — Instrumented indentation test for hardness and materials parameters. 2002.

- [28] Mori T, Tanaka K. Average stress in matrix and average elastic energy of materials with misfitting inclusions. *Acta metallurgica*. 1973;21(5):571-4.
- [29] Benveniste Y. A new approach to the application of Mori-Tanaka's theory in composite materials. *Mechanics of materials*. 1987;6(2):147-57.
- [30] Mure T. Micromechanics of defects in solids. 1987:75-91.
- [31] Sevostianov I, Kachanov M. Compliance Tensors of Ellipsoidal Inclusions. *International Journal of Fracture*. 1999;96(1):3-7.
- [32] Beaudoin J, Feldman R, Tumidajski P. Pore structure of hardened Portland cement pastes and its influence on properties. *Advanced Cement Based Materials*. 1994;1(5):224-36.
- [33] Neville AM. *Properties of concrete* 1995.
- [34] Shavshukov V, Tashkinov A, Strzhemechny Y, Hui D. Modelling of pseudoplastic deformation of carbon/carbon composites with a pyrocarbon matrix. *Modelling and Simulation in Materials Science and Engineering*. 2008;16(5):055001.
- [35] Dement'ev S, Zabolotskii A, Romanovich I, Prokof'ev S, Salibekov S. Reaction of carbon fibers with magnesium. *Soviet Powder Metallurgy and Metal Ceramics*. 1977;16(3):197-200.
- [36] Zhu Y, Zhou B, He G, Zheng Z. A Statistical Theory of Composite Materials Strength. *Journal of Composite Materials*. 1989;23(23):280-7.
- [37] Sun J, Li H, Feng L, Jia Y, Song Q, Li K. A novel treatment of carbon fibers with improving tensile strength to synthesize evenly distributed carbon nanotubes on their surface. *Applied Surface Science*. 2017;403:95-102.
- [38] Daniels H. The statistical theory of the strength of bundles of threads. I. *Proceedings of the Royal Society of London A: Mathematical, Physical and Engineering Sciences: The Royal Society*; 1945. p. 405-35.
- [39] Davila CG, Camanho PP, Rose CA. Failure criteria for FRP laminates. *Journal of Composite materials*. 2005;39(4):323-45.
- [40] Li S, Sitnikova E, Liang Y, Kaddour A-S. The Tsai-Wu failure criterion rationalised in the context of UD composites. *Composites Part A: Appl Sci Manuf*. 2017;102(Supplement C):207-17.
- [41] Benzeggagh ML, Kenane M. Measurement of mixed-mode delamination fracture toughness of unidirectional glass/epoxy composites with mixed-mode bending apparatus. *Compos Sci Technol*. 1996;56(4):439-49.
- [42] Li B, Li Y, Su J. A combined interface element to simulate interfacial fracture of laminated shell structures. *Composites Part B: Engineering*. 2014;58:217-27.
- [43] Moet A, Minick J. Fracture toughness of carbon/carbon composites. Final report, 1 Apr 89-30 Jun 91. *Computer Aided Chemical Engineering*. 1991;29(6):1170-4.
- [44] Tzeng S-S, Lin W-C. Mechanical behavior of two-dimensional carbon/carbon composites with interfacial carbon layers. *Carbon*. 1999;37(12):2011-9.
- [45] Budiansky B, Fleck NA. Compressive failure of fibre composites. *J Mech and Phys Solids*. 1993;41(1):183-211.
- [46] Huang Z-m. Micromechanical prediction of ultimate strength of transversely isotropic fibrous composites. *Intl J Solids Struct*. 2001;38(22):4147-72.

- [47] Dimitrienko Y. Modelling of the mechanical properties of composite materials at high temperatures: Part 2. Properties of unidirectional composites. *Applied Composite Materials*. 1997;4(4):239-61.
- [48] Dimitrienko Y. Modelling of the mechanical properties of composite materials at high temperatures: Part 1. Matrix and fibers. *Applied Composite Materials*. 1997;4(4):219-37.
- [49] ABAQUS/Standard. ABAQUS scripting/analysis user's manual Version 6.14-1 RI: ABAQUS Inc. 2014.
- [50] Zhang MY, Li KZ, Shi XH, Guo LJ, Sun JJ, Shen QL. Effects of low-temperature thermal cycling treatment on the microstructures, mechanical properties and oxidation resistance of C/C-ZrC-SiC composites. *Journal of Alloys & Compounds*. 2017.
- [51] Aggelopoulos ES, Righiniotis TD, Chryssanthopoulos MK. Debonding of adhesively bonded composite patch repairs of cracked steel members. *Composites Part B Engineering*. 2011;42(5):1262-70.
- [52] Hoiseth K, Qu J. Cracking paths at the ply interface in a cross-ply laminate. *Composites Part B Engineering*. 2003;34(5):437-45.
- [53] Dvorak GJ, Laws N. Analysis of Progressive Matrix Cracking In Composite Laminates II. First Ply Failure. *Journal of Composite Materials*. 1987;21(4):309-29.